PHYSICAL REVIEW D **90,** 103532 (2014)

Simple proposal for radial 3D needlets

C. Durastanti,[1,*] Y. Fantaye,[1,†] F. Hansen,[2,‡] D. Marinucci,[1,§] and I. Z. Pesenson[3,‖]

[1]*Dipartimento di Matematica, Universit di Roma "Tor Vergata", Via della Ricerca Scientifica 1, I-00133 Roma, Italy*

[2]*Institute of Theoretical Astrophysics, University of Oslo, P.O. Box 1029 Blindern, 0315 Oslo, Norway*

[3]*Department of Mathematics, Temple University, Philadelphia, Pennsylvania 19122, USA*

(Received 7 August 2014; published 26 November 2014)

We present here a simple construction of a wavelet system for the three-dimensional ball, which we label *radial 3D needlets*. The construction envisages a data collection environment in which an observer located at the center of the ball is surrounded by concentric spheres with the same pixelization at different radial distances, for any given resolution. The system is then obtained by weighting the projector operator built on the corresponding set of eigenfunctions and performing a discretization step which turns out to be computationally very convenient. The resulting wavelets can be shown to have very good localization properties in the real and harmonic domain; their implementation is computationally very convenient, and they allow for exact reconstruction as they form a tight frame system. Our theoretical results are supported by an extensive numerical analysis.

DOI: 10.1103/PhysRevD.90.103532 PACS numbers: 98.80.-k, 07.05.Rm, 95.75.Mn

I. INTRODUCTION

The last decade has represented a golden era for cosmology; a flood of data with unprecedented accuracy has become available on such diverse fields as the cosmic microwave background (WMAP, Planck, SPT, and ACT; see, for instance, Refs. [1–4] and references therein), ultrahigh energy cosmic rays (see Ref. [5]), gamma rays (Fermi, Agile, ARGO-YBJ+; see Refs. [6–8]), neutrinos (see Ref. [9]), and many others. Many of these experiments have produced full-sky surveys, and basically all of them have been characterized by fields of view covering thousands of square degrees. In such circumstances, data analysis methods based on flat sky approximations have become unsatisfactory, and a large amount of effort has been devoted to the development of procedures that take fully into account the spherical nature of collected data.

As is well known, Fourier analysis is an extremely powerful method for data analysis and computation; in a spherical context, Fourier analysis corresponds to the spherical harmonics dictionary, which is now fully implemented in very efficient and complete packages such as HEALpix; see Ref. [10]. For most astrophysical applications, however, standard Fourier analysis may often be inadequate due to the lack of localization properties in the real domain; because of this, spherical harmonics cannot easily handle the presence of huge regions of masked data, nor can they be used to investigate local features such as asymmetries and anisotropies or the search for point sources.

As a consequence, several methods based on spherical wavelets have become quite popular in astrophysical data analysis; see, for instance, Refs. [11–24] and also Ref. [25] for a review. These procedures have been applied to a huge variety of different problems, including, for instance, point source detection in Gamma ray data (see Refs. [26,27]), testing for non-Gaussianity (see Refs. [13,21,28,29]), searching for asymmetries and local features (see Refs. [20,30,31]), point source subtraction on cosmic microwave background data (see Ref. [32]), map making and component separation (see Refs. [33–36]), and several others.

The next decade will probably experience an even more amazing improvement in observational data. Huge surveys are being planned or are already at the implementation stage, with many of them aimed at the investigation of the large scale structure of the Universe and the investigation of dark energy and dark matter; for instance, a large international collaboration is fostering the implementation of the Euclid satellite mission, aimed at a deep analysis of weak gravitational lensing on nearly half of the celestial sky (see, for instance, Ref. [37]). These observational data are also complemented by N-body simulation efforts (see Ref. [38]) aimed at the generation of a realistic three-dimensional model of the current large scale structure of the Universe. From the point of view of data analysis, these data naturally entail a three-dimensional structure, which calls for suitable techniques of data analysis.

In view of the previous discussion, it is easy to understand the motivation to develop wavelet systems on the three-dimensional ball, extending those already available on the sphere. Indeed, some important efforts have already

*durastan@axp.mat.uniroma2.it
†fantaye@axp.mat.uniroma2.it
‡f.k.hansen@astro.uio.no
§marinucc@mat.uniroma2.it
‖pesenson@temple.edu

been spent in this direction, especially in the last few years. Some attempts outside the astrophysical community have been provided by Refs. [39–41]; however, the first two proposals are developed in a continuous setting and do not seem to address discretization issues and the implementation of an exact reconstruction formula. On the other hand, in Ref. [41] the authors proceeded by projecting the three-dimensional ball into a unit sphere in four dimensions and then developing the corresponding spherical needlet construction in the latter space. While this approach is mathematically intriguing, to the best of our knowledge, it has not led to a practical implementation, at least in an astrophysical context. This may be due to some difficulties in handling the required combination of Jacobi polynomials and the lack of explicit recipes for cubature points in this context; moreover, the projection of the unit ball on a unit sphere in higher dimensions may induce some local anisotropies, of which the effect still needs to be investigated in an astrophysical context.

Within the astrophysical community, some important proposals for the construction of three-dimensional wavelets have been advocated by Refs. [42] and [43]. In the former paper, the authors propose using a frequency filter on the Fourier–Bessel transform of the three-dimensional field. The proposal by Ref. [43] also concentrates on Fourier–Bessel transforms and is mainly aimed at the construction of a proper set of cubature points and weights on the radial part. This is in practice a rather difficult task; while it is theoretically known that the cubature points can be taken to be the zeros of Bessel functions of increasing degrees, in practice these points are not available explicitly, and the related computations may be quite challenging. To overcome this issue, in Ref. [43], a very interesting solution is advocated; more precisely, the authors start by constructing an exact transform on the radial part using damped Laguerre polynomials, which allow for an exact quadrature rule. Combining this procedure with the standard spherical transform, they obtain an exact three-dimensional decomposition named the Fourier–Laguerre transform. Their final proposal, the so-called flaglet transform, is then obtained by an explicit projection onto the Bessel family (e.g., a form of harmonic tiling on the Fourier–Laguerre transform); this approach is computationally feasible and exhibits very good accuracy properties from the numerical point of view.

Our starting point here is to some extent related and quite explicitly rooted in the astrophysical applications we have in mind. In particular, we envisage a situation in which an observer located at the center of a ball is collecting data; e.g., we assume that she/he is observing a family of concentric spheres centred at the origin. At a given resolution level, the pixelization on each of these spheres is assumed to be the same, no matter their radial distance from the origin—this seems a rather realistic representation of astrophysical experiments, although of course it implies that with respect to Euclidean distance the sampling is finer for points located closer to the observer. In this sense, our construction has an implicit radial symmetry that we exploit quite fully; in particular, we view the ball of radius R as a manifold $M = [0, R] \times S^2$, and we modify the standard spherical Laplacian so that the distance between two points on the same spherical shell depends only on the angular component and not on the radius of the shell. The corresponding eigenfunctions have very simple expressions in terms of trigonometric polynomials and spherical harmonics; our system (which we label *3D radial needlets*) is then built out of the same procedures as for needlets on the sphere, namely, convolution of a projection operator by means of a smooth window function $b(\cdot)$ and discretization by means of an explicitly provided set of cubature points. Concerning the latter, cubature points and weights arise very simply from the tensor products of cubature points on the sphere (as provided by HEALpix in Ref. [10], for instance) and a uniform discretization on the radial part, which is enough for exact integration of trigonometric polynomials. One possible concern with this approach is that we are implicitly enforcing periodicity through the use of complex exponentials; however, for practical astrophysical applications, this issue can be addressed using zero padding, which ensures periodic boundary conditions (of course, observational data are only available in a finite redshift range).

We believe the present proposal enjoys some important advantages, such as the following:

(1) Very good localization properties (in the suitable distance, as motivated before); these properties can be established in a fully rigorous mathematical way, exploiting previous results on the construction of wavelets for general compact manifolds in Ref. [44]; see also Ref. [45].
(2) An exact reconstruction formula for band-limited functions, a consequence of the so-called tight frame property; the latter property has independent interest, for instance, for the estimation of a binned spectral density by means of needlet coefficients (see Ref. [46] for analogous results in the spherical case).
(3) A computationally simple and effective implementation scheme, entailing uniform discretization and the exploitation of existing packages.
(4) A natural embedding into experimental designs that appear quite realistic from an astrophysical point of view, as discussed earlier.

The construction and these properties are discussed in more detail in the rest of this paper; we note that the same ideas can be simply extended to cover the case of spin valued functions, along the same lines as done for standard 2D needlets by Refs. [47,48]; these extensions may be of interest to cover forthcoming data on weak gravitational lensing (e.g., Ref. [37]).

The paper is divided as follows. Section II presents the background material on our embedding of the three-dimensional ball, related Fourier analysis, and discretization issues. Section 3 presents the 3D radial needlets construction in detail. Section 4 discusses the comparison with possible alternative proposals. Section 5 presents our numerical evidence, while some technical computations are collected in the Appendix.

II. BASIC FRAMEWORK

As mentioned in the Introduction and discussed at length also in other papers (Refs. [43,49]), in an astrophysical framework, data collection on the ball is characterized by a marked asymmetry between the radial part and the spherical component. Indeed, it is well known that for astrophysical data sets observations at a growing radial distance correspond to events at higher redshift, which have hence occurred farther away in time, not only in space; data at different redshifts correspond to different epochs of the Universe and are hence the outcome of different physical conditions. From the experimental point of view, the signal-to-noise ratio is strongly influenced by radial distance; for instance, a strong selection bias is introduced as higher and higher intrinsic luminosity is needed to observe objects at growing redshift. The asymmetry between the radial and spherical components is also reproduced in data storing mechanisms, which typically adopt independent discretization/pixelization schemes for the two components.

In view of these considerations, it seems natural and convenient to represent functions/observations on the three-dimensional ball $\mathcal{B}_R = \{(x_1, x_2, x_3) : x_1^2 + x_2^2 + x_3^2 \leq R\}$ as being defined on a family of concentric spheres (shells), indexed by a continuous radial parameter (i.e., a growing redshift); here, the radius R of the ball can be taken to represent the highest redshift value z in the catalog being analyzed, $R = z_{\max}$. In the sequel, we shall work with spherical coordinates (r, θ, φ); for notational convenience, we take $r = 2\pi z/R$ so that $r \in [0, 2\pi]$. Formally, this means we shall focus on the manifold $M = (0, 2\pi] \times S^2$ and on the product space

$$L^2(M, d\mu) = L^2((0, 2\pi], dr) \otimes L^2(S^2, d\sigma),$$

where $d\mu = dr d\sigma$, $d\sigma = (4\pi)^{-1} \sin\theta d\theta d\phi$ and dr denotes standard Lebesgue measure on the unit interval. This simplifying step is at the basis of our construction; indeed, for our purposes, it will hence be sufficient to construct a tight and localized frame on $L^2(M, d\mu)$, a task that can be easily accomplished as follows.

Recall first that for square-integrable functions on the sphere, e.g., on $L^2(S^2, d\sigma)$, a standard orthonormal basis is provided by the set of spherical harmonics,

$$\{Y_{\ell,m}(\theta, \phi)\}, \qquad \ell = 0, 1, 2, \ldots, \qquad m = -\ell, \ldots, \ell,$$

where $\theta \in [0, \pi]$ and $\varphi \in [0, 2\pi)$. As is well known, the spherical harmonics provide a complete set of eigenfunctions for the spherical Laplacian

$$\Delta_{S^2} = \frac{1}{\sin\theta}\frac{\partial}{\partial\theta}\left(\sin\theta\frac{\partial}{\partial\theta}\right) + \frac{1}{\sin^2\theta}\frac{\partial}{\partial\varphi};$$

indeed,

$$\Delta_{S^2} Y_{\ell,m} = -\ell(\ell+1) Y_{\ell,m}, \qquad \ell = 1, 2, \ldots$$

Hence, for any $f \in L^2(S^2, d\sigma)$, we have

$$f(\omega) = \sum_{\ell \geq 0} \sum_{m=-l}^{l} a_{\ell,m} Y_{\ell,m}(\omega), \qquad \omega \in S^2,$$

where the coefficients $\{a_{\ell m}\}$ are evaluated by

$$a_{\ell,m} = 4\pi \int_{S^2} \bar{Y}_{\ell,m}(\omega) f(\omega) \sigma(d\omega),$$

where for any complex z, $\bar{z}$ denotes its conjugate complex.

On the other hand, for the radial part, we consider the standard Laplacian operator $\frac{\partial^2}{\partial r^2}$, for which an orthonormal family of eigenfunctions is well known to be given, for $n = 0, 1, 2, \ldots$, by

$$\frac{\partial^2}{\partial r^2}(2\pi)^{-\frac{1}{2}} \exp(inr) = -n^2 (2\pi)^{-\frac{1}{2}} \exp(inr).$$

We can hence define a Laplacian on M by

$$\Delta_M := \frac{\partial^2}{\partial r^2} + \Delta_{S^2},$$

e.g.,

$$\Delta_M(\exp(inr) Y_{\ell m}(\omega)) = -e_{n,\ell} \exp(inr) Y_{\ell m}(\omega), \qquad (2.1)$$

where

$$e_{n,\ell} = (n^2 + \ell(\ell+1)).$$

It is interesting to compare the action of Δ_M with the standard Laplacian in spherical coordinates, which is given by

$$\Delta = \frac{1}{r^2}\frac{\partial}{\partial r} r^2 \frac{\partial}{\partial r} + \frac{1}{r^2}\Delta_{S^2}; \qquad (2.2)$$

it can be checked that Δ_M is the Laplace–Beltrami operator that corresponds to the metric tensor

$$g_M = \begin{pmatrix} 1 & 0 & 0 \\ 0 & 1 & 0 \\ 0 & 0 & \sin^2\theta \end{pmatrix},$$

as opposed to the usual Euclidean metric in spherical coordinates,

$$g = \begin{pmatrix} 1 & 0 & 0 \\ 0 & r^2 & 0 \\ 0 & 0 & r^2\sin^2\theta \end{pmatrix}.$$

Likewise, the intrinsic distance between points $x_1 = (r_1, \omega_1) = (r_1, \theta_1, \varphi_1)$ and $x_2 = (r_2, \omega_2) = (r_2, \theta_2, \varphi_2)$, $\omega_1, \omega_2 \in S^2$, $r_1, r_2 \in [0, 2\pi]$, and $x_1, x_2 \in M$, is provided by

$$d_M(x_1, x_2) = \sqrt{(r_1 - r_2)^2 + d^2_{S^2}(\omega_1, \omega_2)}, \tag{2.3}$$

as opposed to Euclidean distance in spherical coordinates,

$$d(x_1, x_2) = \sqrt{(r_1 - r_2)^2 + r_1 r_2 d^2_{S^2}(\omega_1, \omega_2)}. \tag{2.4}$$

In words, in our setting, the distance between two points at a given redshift is simply equal to their angular separation, whatever the redshift; on the contrary, under the Euclidean distance for a given angular separation, the actual distance grows with the radial component. It can be argued that the metric $d_M(\cdot, \cdot)$ is a natural choice for any wavelet construction in which the radial component is decoupled from the spherical one. Given this choice of metric, our construction can be advocated as optimal, in the sense that it is based on the eigenfunctions of the associated Laplacian, and hence can be shown to enjoy excellent localization properties in the real and harmonic domains.

As a consequence of the previous discussion, the family of functions

$$u_{\ell,m,n}(r, \vartheta, \phi) = (2\pi)^{-\frac{1}{2}} \exp(inr) Y_{\ell,m}(\vartheta, \phi) \tag{2.5}$$

provides an orthonormal basis on $L^2(M, d\mu)$; e.g., for any $F \in L^2(M, d\mu)$, the following expansion holds in $L^2(M, d\mu)$,

$$F(r, \vartheta, \phi) = \sum_{\ell \geq 0} \sum_{m=-\ell}^{\ell} \sum_{n \geq 0} a_{\ell,m,n} u_{\ell,m,n}(r, \vartheta, \phi), \tag{2.6}$$

where

$$a_{\ell,m,n} := \langle F, u_{\ell,m,n} \rangle_{L^2(M,d\mu)} = \int_M F(x) \bar{u}_{\ell,m,n}(x) d\mu(x). \tag{2.7}$$

Of course, we can also rewrite (2.1) more compactly as

$$\Delta_M u_{\ell,m,n} = -e_{\ell,n} u_{\ell,m,n}. \tag{2.8}$$

It may be noted that, by taking a trigonometric basis for the radial part, we are implicitly assuming that the functions to reconstruct satisfy periodic boundary conditions. For astrophysical applications, this does not seem to bring in any problem. Indeed, we envisage circumstances in which catalogs are provided within some band of redshift values $0 < z_{\min} < z_{\max}$; periodicity is then obtained by simply padding zero observations at the boundaries.

The final step we need to complete our frame construction is discretization; the procedure is standard and can be outlined as follows. Let Π_Λ be the a set of band-limited functions of order smaller than Λ, i.e., the linear span of the basis elements $\{u_{\ell,m,n}\}$ for which the corresponding eigenvalues are such that $e_{\ell,n} \leq \Lambda$. Given an integer j, there exists a set of points $\aleph_j := \{\xi_{j,q,k} = (r_{j,q}, \theta_{j,k}, \varphi_{j,k})\}$ and positive weights $\{\lambda_{j,q,k}\}$, $1 \leq q \leq Q_j$, $1 \leq k \leq K_j$, such that for all $P \in \Pi_{B^{2j+2}}$ the exact cubature formula

$$\int_M P(x) d\mu(x) = \int_{S^2} \int_0^1 P(r, \theta, \varphi) dr d\sigma(\theta, \varphi) = \sum_{q=1}^{Q_j} \sum_{k=1}^{K_j} P(\xi_{j,q,k}) \lambda_{j,q,k} \tag{2.9}$$

holds, where $\xi_{j,q,k} = (r_{j,q}, \theta_{j,k}, \varphi_{j,k})$ and the cubature points and weights satisfy

$$\lambda_{j,q,k} \approx B^{-3j}, \qquad K_j \approx B^{2j}, \qquad Q_j \approx B^j$$

for $B > 1$ and the notation $x_1 \approx x_2$ means that there exists $c > 0$ such that $c^{-1} x_1 \leq x_2 \leq c x_1$. More explicitly, K_j denotes the pixel cardinality on the spherical part, and Q_j represents the pixel cardinality on the radial part for a given resolution level j. In words, this means that, for such functions, integrals can be evaluated by finite sums over suitable points without any loss of accuracy. The existence of cubature points with the required properties follows immediately from the tensor construction that we described in the previous subsection: in particular, the spherical component $(\theta_{j,k}, \varphi_{j,k})$ can be provided along the same scheme as in Ref. [50], while for practical applications, the highly popular pixelization scheme provided by HEALpix (see Ref. [10]) may be used; on the radial part, cubature points maybe simply taken to be given by $r_{j,q} := \frac{2\pi q}{B^j}$, $q = 0, \ldots, [B^j] - 1$, where $[\cdot]$ denotes the integer part, see Sec. V, and $B > 1$.

III. 3D RADIAL NEEDLETS AND THEIR MAIN PROPERTIES

Having set the basic framework for Fourier analysis and discretization on $L^2(M, d\mu)$, the construction of 3D radial needlets can proceed along very much the same lines as on the sphere or other manifolds (compare Refs. [45,50–54]). More precisely, let us fix a scale parameter $B > 1$, and let $b(u)$, $u \in \mathbb{R}$, be a positive kernel satisfying the following three assumptions:

(1) $b(\cdot)$ has compact support in $[1/B, B]$.
(2) $b(\cdot)$ is infinitely differentiable in $(0, \infty)$.
(3) The following partition of unity property holds:

$$\sum_{j=-\infty}^{\infty} b^2\left(\frac{u}{B^j}\right) = 1, \quad \text{for all } u > 0.$$

In Fig. 1, we show a visualization of $b(\frac{\sqrt{e_{\ell,n}}}{B^j})$ for different needlet frequency j values and $\ell_{\max} = n_{\max} = 200$.

Numerical recipes for the construction of window functions satisfying the three conditions above are now well known to the literature; for instance, in Ref. [19] (see also Ref. [55]), the following procedure is introduced:

(i) STEP 1: Construct the C^∞ function

$$\phi_1(t) = \begin{cases} \exp\left(-\frac{1}{1-t^2}\right) & t \in [-1, 1] \\ 0 & \text{otherwise} \end{cases},$$

compactly supported in $[-1, 1]$.

(ii) STEP 2: Implement the nondecreasing C^∞ function

$$\phi_2(u) = \frac{\int_{-1}^{u} \phi_1(t)dt}{\int_{-1}^{1} \phi_1(t)dt},$$

satisfying $\phi_2(-1) = 0$; $\phi_2(1) = 1$.

(iii) STEP 3: Construct the function

$$\phi_3(t) = \begin{cases} 1 & t \in [0, 1/B] \\ \phi_2\left(1 - \frac{2B}{B-1}\left(t - \frac{1}{B}\right)\right) & t \in (1/B, 1] \\ 0 & t \in (1, \infty) \end{cases}.$$

(iv) STEP 4: Define, for $u \in \mathbb{R}$,

$$b^2(u) = \phi_3\left(\frac{u}{B}\right) - \phi_3(u).$$

Now recall that $e_{\ell,n} = n^2 + \ell(\ell+1)$, and let the symbol $[\ell, n]_j$ denote the pairs of ℓ and n such that $e_{\ell,n}$ is bounded above and below, respectively, by $B^{2(j+1)}$ and $B^{2(j-1)}$, i.e.,

$$[\ell, n]_j = \{l, n\colon B^{2(j-1)} \le e_{\ell,n} \le B^{2(j+1)}\}.$$

We have the following:

Defination 1: For $x = (r, \vartheta, \varphi) \in M$, the radial 3D-needlets basis is defined by

$$\Phi_{j,q,k}(x) = \sqrt{\lambda_{j,q,k}} \sum_{[\ell,n]_j} \sum_{m=-\ell}^{\ell} b\left(\frac{\sqrt{e_{\ell,n}}}{B^j}\right) \times \bar{u}_{\ell,m,n}(\xi_{j,q,k}) u_{\ell,m,n}(x), \tag{3.1}$$

where $\lambda_{j,q,k}$ and $\xi_{j,q,k}$ denote, respectively, the pixel volume and the pixel center.

Analogously to the related constructions on the sphere or on other manifolds, radial 3D needlets can be viewed as the convolution of the projector operator

$$Z_{\ell n}(\xi_{j,q,k}, x) = \sum_m \bar{u}_{\ell,m,n}(x) u_{\ell,m,n}(\xi_{j,q,k})$$

with the window function $b(\cdot)$. The properties of this system are to some extent analogous to the related construction on the sphere, as illustrated below.

A. Tight frame property

Let us first recall the notion of tight frame, which is defined to be a countable set of functions $\{e_i\}$ such that

$$\sum_i \beta_i^2(f) = \int_M f(x)^2 dx,$$

where the coefficients $\beta_i(f)$ are defined by

$$\beta_i(f) = \int f(x) e_i(x) dx, \tag{3.2}$$

so that the "energy" of the function f is fully conserved in the collection of β_i's; we refer, for instance, to Refs. [56,57] and the references therein for more details and discussions. In words, a tight frame can be basically seen as a (possibly

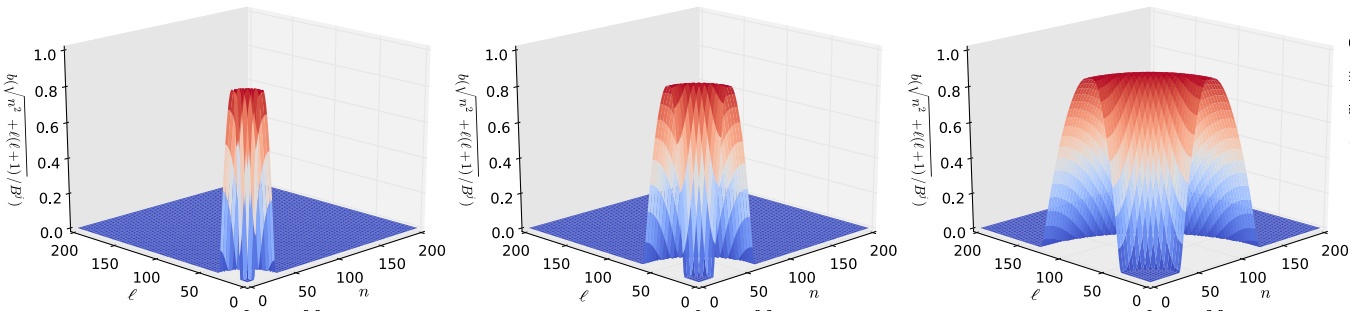

FIG. 1 (color online). 3D needlet window functions $b(\frac{\sqrt{e_{\ell,n}}}{B^j})$: $j = 4$ (left panel), $j = 5$ (middle panel), and $j = 6$ (right panel).

redundant) basis; indeed, we recall that tight frames enjoy the same reconstruction property as standard orthonormal systems, e.g.,

$$f = \sum_i \beta_i(f) e_i,$$

with equality holding in the L^2 sense.

It is a straightforward consequence of the previous construction that the set $\{\Phi_{j,q,k}\}$ describes a tight frame over $L^2(M, d\mu)$, with tightness constant equal to 1, so that an exact reconstruction formula holds in this space; the details of the derivation of this result are collected in the Appendix. Indeed, let $F \in L^2(M, d\mu)$, i.e., the space of functions that have finite norm $\|.\|^2_{L^2(M)}$, where

$$\|F\|^2_{L^2(M,d\mu)} := \int_0^{2\pi} \int_{S^2} F^2(r, \vartheta, \varphi) \sin\vartheta dr d\vartheta d\varphi. \quad (3.3)$$

The 3D-needlet coefficients are defined as

$$\beta_{j,q,k} := \beta_{j,q,k}(F) = \int F \Phi_{j,q,k} d\mu$$

or, more explicitly,

$$\beta_{j,q,k} = \sqrt{\lambda_{j,q,k}} \sum_{[\ell,n]_j} \sum_{m=-\ell}^{\ell} b\left(\frac{\sqrt{e_{\ell,n}}}{B^j}\right) a_{\ell,m,n} u_{\ell,m,n}(\xi_{j,q,k}), \quad (3.4)$$

where $a_{\ell,m,n}$ is given by (2.7). The tight frame property then gives

$$\|F\|^2_{L_2(M,d\mu)} = \sum_{j\geq 0} \sum_{q=1}^{Q_j} \sum_{k=1}^{K_j} |\beta_{j,q,k}|^2.$$

This property implies also the reconstruction formula

$$F(x) = \sum_{j\geq 0} \sum_{k=1}^{K_j} \sum_{q=1}^{Q_j} \beta_{j,q,k} \Phi_{j,q,k}(x); \quad (3.5)$$

see the Appendix for more discussion and some technical details. Note also that all radial 3D needlets have zero mean, and hence they cannot represent signals with nonzero mean. However, for practical purposes, this does not represent a concern since many astrophysical signals of interest are indeed zero mean, representing the perturbations of a signal around an average value. In any case, the mean can be added "by hand" if needed, by simply adding constants.

There are some important statistical applications of the tight frame property. First, the reconstruction property allows the implementation of denoising and image reconstruction techniques, for instance, on the basis of the universally known thresholding paradigm (see, for instance, Refs. [46,58,59]); in view of the localization properties discussed in the following paragraph, such denoising techniques will enjoy statistical optimality properties, in the sense of minimizing the expected value of the reconstruction error, defined by

$$\mathbb{E}\left[\|\hat{F} - F\|^2_{L^2(M,d\mu)}\right] = \mathbb{E}\left[\int_M (\hat{F}(x) - F(x))^2 d\mu(x)\right].$$

Here, $\mathbb{E}[\cdot]$ denotes the expected value and $\hat{F}$ the reconstructed function in the presence of additive noise with standard properties. It is important to stress that this reconstruction error is measured according to the norm introduced in (3.3), rather than the usual Euclidean measure in spherical coordinates, where integration is performed with respect to the factor $r^2 \sin\vartheta dr d\vartheta d\varphi$. In practical terms, this means that the observations at lower redshift are given a higher weight when performing image denoising; this appears a rather reasonable strategy, as most astrophysical catalogs are more complete and less noisy at lower redshift.

We also note that the tight frame property allows an estimator for the averaged power spectrum of random fields to be constructed by means of the squared needlet coefficients, along the same lines as, for instance, Ref. [60] in the spherical case. More details and further investigations on all these issues are left for future research.

B. Localization properties

It is immediately seen that the functions $\{\Phi_{j,q,k}(\cdot)\}$ are compactly supported in the harmonic domain; indeed, for any fixed j, as argued before, we have that $b(u)$ is nonzero for $u \in (B^{-1}, B)$, and hence it follows that $b(\frac{\sqrt{e_{\ell,n}}}{B^j}) \neq 0$ only for $e_{\ell,n} \in [B^{2(j-1)}, B^{2(j+1)}]$. For instance, for $B = \sqrt{2}$ and $j = 4$, we have $8 \leq e_{\ell,n} \leq 32$, allowing for the pairs

$$(\ell, n) = (1,3), (1,4), (1,5), (2,2), (2,3), (2,4), \ldots, (5,1).$$

It is also easy to establish localization in the real domain by means of general results on localization of needlet-type constructions for smooth manifolds. In particular, it follows from theorem 2.2 in Ref. [44], see also Ref. [54], that for all $\tau \in \mathbb{N}$ there exists constants c_τ such that

$$|\Phi_{j,q,k}(x)| \leq \frac{c_\tau B^{\frac{3}{2}j}}{(1 + B^j d_M(x, \xi_{j,q,k}))^\tau}, \quad (3.6)$$

uniformly over j, q, k, and x. It is very important to notice that the distance at the denominator is provided by equation (2.3).

An important consequence of localization can be derived on the behavior of the L^p norms for the functions $\{\Phi_{jqk}(\cdot)\}$. In particular, it can be proved by standard arguments (as, for instance, in Ref. [50]) that, for all $1 \leq p < \infty$,

$$\|\Phi_{j,q,k}\|_{L^p(M,d\mu)} \approx B^{\frac{3}{2}(1-\frac{2}{p})j}, \tag{3.7}$$

while

$$\|\Phi_{j,q,k}\|_{L^\infty(M,d\mu)} \approx B^{\frac{3}{2}j}.$$

The result is consistent with the general characterization for the L^p norm of spherical needlets on S^d, which is well known to be given by $\|\psi_{j,k}\|^p_{L^p(S^d)} \approx B^{\frac{d}{2}(p-2)j}$; here, of course, $d = 3$. The proof is completely standard and hence omitted; we only remark that this characterization of L^p properties plays a fundamental role when investigating the optimality of denoising and image reconstruction techniques based on wavelet thresholding; see again Ref. [46] for further references and discussion.

IV. COMPARISON WITH ALTERNATIVE CONSTRUCTIONS

The ingredients for the construction of localized tight frames on a compact manifold are now well understood; one starts from a family of eigenfunctions and the associated projection kernel, then considers a window function to average these projectors over a bounded subset of frequencies, then proceeds to discretization by means of a suitable set of cubature points and weights (see again, for instance, Refs. [44,45,50–53,61]). The localization and tight frame properties are then easy consequences of general results. A natural question then arises: what would be the alternative properties of a construction based on a different choice of eigenfunctions, corresponding, for instance, to the standard Laplacian in spherical coordinates [e.g., (2.2) rather than (2.1)]?. Indeed, a full system of eigenfunctions for the Laplacian in spherical coordinates is well known to be given by

$$E_{\ell,m,k}(r,\omega) = \sqrt{\frac{2}{\pi}}\frac{J_{\ell+\frac{1}{2}}(kr)}{\sqrt{kr}}Y_{\ell,m}(\omega), \qquad r \in [0,1], \quad \omega \in S^2,$$

which can be discretized imposing the boundary conditions $E_{\ell,m,k}(1,\omega) \equiv 0$, yielding the family $\{E_{\ell,m,k_{\ell p}}(r,\omega)\}$, where $k_{\ell p}$ are the zeros of the Bessel function $J_{\ell+\frac{1}{2}}(\cdot)$ in the interval (0,1). Writing $e(\ell, k_{\ell_p})$ for the corresponding set of eigenvalues, a needlet-type construction would then lead to the proposal

$$\Psi_{j,q,k}(r,\omega) = \sqrt{\lambda_{j,q,k}}\sum_{\ell,m}\sum_{k_{\ell p}} b\left(\frac{\sqrt{e(\ell,k_{\ell_p})}}{B^j}\right) \times E_{\ell,m,k_{\ell_p}}(r,\omega)E_{\ell,m,k_{\ell_p}}(r_q,\omega_{j,k}),$$

which is close to the starting point of the construction in Ref. [43], the main difference being that their weight function is actually a product of a radial and spherical part, and its argument is not immediately related to the eigenvalues of the summed eigenfunctions (see also Ref. [42] for 3D isotropic wavelets based on Bessel functions). It is then easy to show that $\Psi_{j,q,k}(\cdot,\cdot)$ enjoys a related form of localization property; namely, for all $\tau \in \mathbb{N}$, there exists constants c_τ such that

$$|\Psi_{j,q,k}(x)| \le \frac{c_\tau B^{\frac{3}{2}j}}{(1 + B^j d(x,\xi_{j,q,k}))^\tau}, \tag{4.1}$$

where $x = (r,\omega)$, $\xi_{j,q,k} = (r_q, \xi_{jk})$, and $d(\cdot,\cdot)$ denotes as before standard Euclidean distance. It is then important to stress the different merits of this construction, with respect to the one on which we focused earlier:

(1) For the system $\{\Psi_{j,q,k}\}$, distances are evaluated with a standard Euclidean metric, and the center of the ball represents a mere choice of coordinates, e.g., the radial part depends just on the choice of coordinate and does not necessarily correspond to a specific physical meaning.
(2) For the system $\{\Phi_{j,q,k}\}$, distances are very much determined by the choice of the center, and the radial part does have a specific interpretation, e.g., the distance to the observer.

The rationale underlying merit 2 was already explained earlier in this paper; we envisage a situation in which an observer located at the center of a ball observes a surrounding Universe made up of concentric spheres having the same pixelizations. As a consequence, "closer" spheres, e.g., those corresponding to smaller radii, are observed at the same angular resolution as more distant ones—in Euclidean coordinates, this obviously means that the sampling is finer. Our construction of radial needlets is simply reflecting this basic feature; as a consequence, for any given frequency, needlets are more localized in proper distance for points located in spheres closer to the observer. This may appear quite rational, to the extent in which for these closer regions the signal-to-noise ratio is higher and hence the reconstruction may proceed to finer details than in the outer regions. The practical performance of these ideas is tested in the section to follow.

V. NUMERICAL EVIDENCE

In this section, we will describe the numerical implementation of the algorithm developed in this paper. As far as the spherical component is concerned, our code exploits the well-tested HEALpix pixelization code (see Ref. [10]), while for the radial part, we use an equidistant pixelization, which is extensively tested below. To investigate the numerical stability and precision properties of the construction we propose, we shall analyze an input

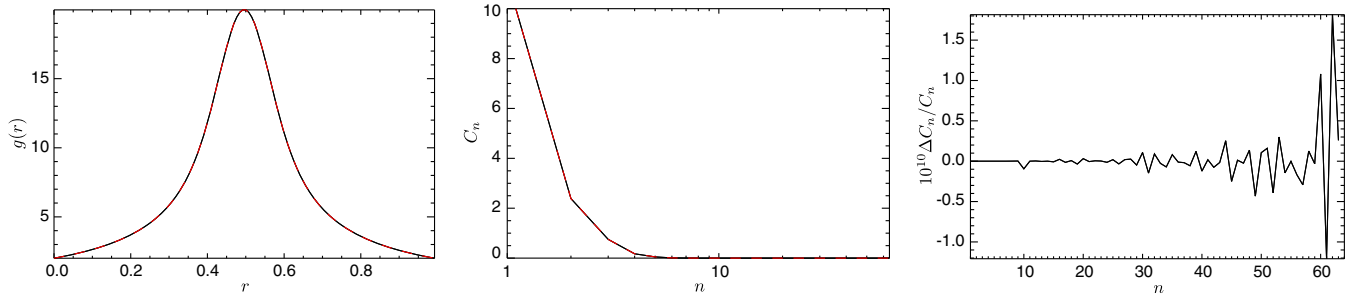

FIG. 2 (color online). Radial line synthesis and analysis: the input (black curve) and reconstructed (red curve—overlapping with the black curve) radial function $g(r)$ (left panel) and radial power spectra C_n (middle panel) and the fractional difference between the input and reconstructed power spectra (right panel). Note that the y axis of the fractional difference panel is multiplied by 10^{10}.

band-limited function on the ball that we simulate using a radial and angular test power spectrum.

All of our tests in this paper are carried out on a 2.40 GHz Core i7-4700MQ processor with 8 GB of RAM. The accuracy of our ball harmonic transform routines is largely dependent on HEALpix's "map2alm_iterative" iteration orders—it is used to transform each spherical shell map to spherical harmonic coefficients, $a_{\ell m}(r)$. As a compromise between speed and accuracy, throughout this paper, we fixed iter_order $= 4$ when we call map2alm_iterative.

A. Radial reconstruction

Given a function $g \in L^2([0, 2\pi], dr)$, we obtain its radial harmonic coefficients by decomposing it in terms of radial eigenfunctions, i.e., for $n = 1, 2, \ldots$,

$$a_n = \int_0^{2\pi} g(r) \frac{\exp(-inr)}{\sqrt{2\pi}} dr, \tag{5.1}$$

The reconstruction of the input function can then be obtained via

$$g(r) = \sum_{n=0}^{\infty} a_n \frac{\exp(inr)}{\sqrt{2\pi}}. \tag{5.2}$$

Given a sampling of $g(r)$ at N_r points, (5.1) and (5.2) can be efficiently solved by forward and backward discrete Fourier transforms. We used the fast Fourier transform (FFT) algorithm implemented in the HEALpix package.

To test our radial integration, we used as an input a Gaussian $g(r)$ function shown in black color in the left panel of Fig. 2. The r grid is normalized, has a range [0,1], and is sampled at $N_r = 128$ points. Using a forward FFT, we obtained the radial power spectrum, $C_n = |a_n|^2$, which is shown in black color in the middle panel of the same figure. We evaluated C_n up to the Nyquist frequency $n_{\max} = 64$. After performing the forward and backward transformation, the reconstructed $g(r)$ and C_n are overplotted in the respective figures—they are not visible because the two curves are almost identical. The fractional difference between the original and reconstructed power spectra are shown in the right-hand side of Fig. 2. The differences are basically in the same order of the floating point precision. This validates our radial analysis and synthesis routines.

B. Discretization of functions on the unit ball

To describe the reconstruction of a band-limited function through the pixelization introduced here, we start from an angular power spectrum C_ℓ that is derived from the CAMB [62] ΛCDM 3D matter power spectrum at redshift $z = 0.5$ and projected to two dimensions through Limber approximation; using HEALpix, we then generated a set of random spherical harmonic coefficients from this power spectrum. We arbitrarily fixed the maximum angular multipole to $\ell_{\max} = 120$. For the radial component, we used the $g(r)$ and a_n described in the previous section. We then computed the input ball harmonic coefficients as $a_{lmn} = a_{lm} * a_n$; the desired function on the 3D ball is then obtained by evaluating it at $N_r = 128$ radial points and HEALpix $N_{\text{side}} = 64$ angular pixels. Our numerical 3D grid has a total of $N_{\text{pix}} = N_r * 12 * N_{\text{side}}^2$ pixels. We stress again that our main interest here is to test the accuracy of the codes, so at this stage, we are not concerned with the physical interest of the functions to be reconstructed; the analysis of more physically motivated models, such as, for instance, maps from N-body simulations will be reported in another paper.

In a similar spirit to the highly popular spherical algorithms proposed by Ref. [10], we have developed the ball equivalent of the HEALpix *alm2map* and *map2alm* codes, which are named *almn2ball* and *ball2almn*. These two routines, respectively, solve the analysis and synthesis equations of (2.7) and (2.6). Equivalently, we have *ball2beta* and *beta2ball* to solve Eqs. (3.4) and (3.5), which are, respectively, performing needlet space analysis and synthesis. We have optimized these codes so that they are fast and run either in serial or parallel mode; we have fully exploited the rigorously tested and well known HEALpix routines so that researchers familiar with HEALpix should

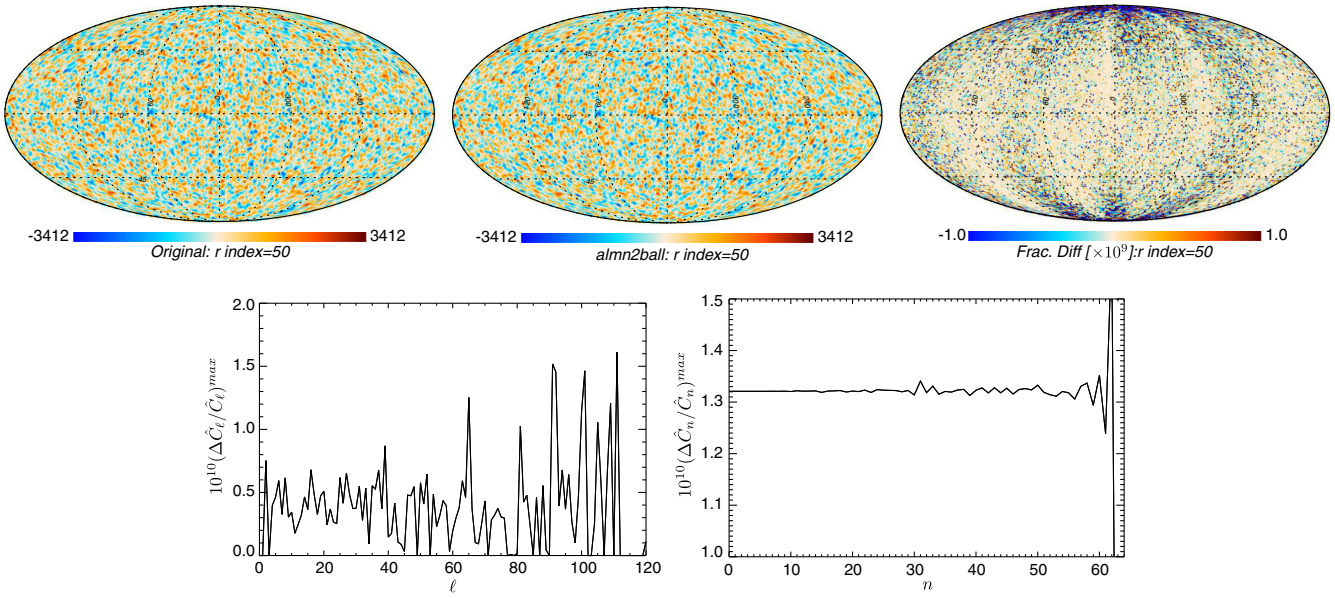

FIG. 3 (color online). Harmonic space synthesis and analysis: input function at the 51st shell (top left), reconstructed function at the 51st shell (top middle), and difference between input and reconstructed functions at the 51st shell (top right). The bottom panels show the maximum fractional difference in the angular (bottom left) and radial (bottom right) power spectra, as defined in Eq. (5.4).

find our code rather intuitive. The modularity of our code, moreover, means that adapting our routines to any other pixelization packages will be straightforward.[1]

To test the accuracy of our code, both in harmonic and real space, in the upper panel of Fig. 3, we show the original and reconstructed function as well as their fractional difference on the unit ball sliced at the 50th radial shell. In the bottom panel, we show the maximal fractional difference in the radial and angular power spectra, which are obtained as

$$\hat{C}_\ell = \frac{1}{n_{\max}} \sum_n \frac{1}{(2\ell+1)} \sum_m |a_{\ell mn}|^2, \tag{5.3}$$

$$\hat{C}_n = \frac{1}{\ell_{\max}} \sum_l \frac{1}{(2\ell+1)} \sum_m |a_{\ell mn}|^2. \tag{5.4}$$

From the real-space and power spectra fractional difference plots, we see that the residuals are very small, in the order of 10^{-9}, and are comparable to HEALpix's accuracy.

C. Radial 3D-needlet synthesis and analysis

Here, we start from the $a_{\ell,m,n}$ coefficients obtained from the previous section analysis, and we compute the needlet coefficients $\beta_{j,q,k}$ through our routine *almn2beta*, which implements (3.1). Optionally, one can start directly from the discretization of the function on the ball and call *ball2beta* to get $\beta_{j,q,k}$ directly. The needlet parameters we use in this analysis are $j = 0, 1, \ldots N_j - 1$, $q = 0, 1, \ldots, Q_j$, $n_k = 0, 1, \ldots, K_j - 1$, where $N_j = 7$, $Q_j = N_r = 256$, and $K_j = 12 * 64^2$. To reconstruct the function on the ball from the needlet coefficients. we call *beta2ball*.

The pixel by pixel and harmonic space accuracy of the function reconstructed from needlet coefficients is very similar to that of the function reconstructed just from the $a_{\ell,m,n}$ coefficients, thus providing some reassuring evidence on the accuracy of the algorithm. An example of the angular and radial needlet components is shown in Fig. 4. The jth needlet component maps have a compact support on the range of combined radial and angular multipoles such that $B^{j-1} < \sqrt{\ell(\ell+1)+n^2} < B^{j+1}$. As mentioned earlier, further evidence on simulations with more realistic experimental conditions is left to future research.

The accuracy and speed of our analysis (almn2ball) and synthesis (ball2almn) implementations are shown in Fig. 5. For an easy comparison with other wavelets on the ball implementations, e.g., Ref. [43], we measure the numerical accuracy by computing the maximal difference between the input and reconstructed harmonic coefficients, $\max(|a_{\ell mn} - a^{\text{rec}}_{\ell mn}|)$; and we measure the speed by taking the average time it takes to do analysis and synthesis, $(t_{\text{analysis}} + t_{\text{synthesis}})/2$. In Fig. 5, both of these metrics are shown as a function of total number of pixels, $N_{\text{pix}} = N_r * 12 * N^2_{\text{side}}$. The *black curves* in the figures correspond to a fixed number of angular pixels, set by HEALpix $N_{\text{side}} = 256$, and an increasing number of radial pixels $N_r = 64, 128, 256, 512, 1024$, while the *red curves* are for a fixed $N_r = 64$ and $N_{\text{side}} = 64, 128, 256, 512, 1024$. The maximum radial and angular

[1]Our codes will be public at https://github.com/yabebalFantaye/Radial3Dneedlet.git.

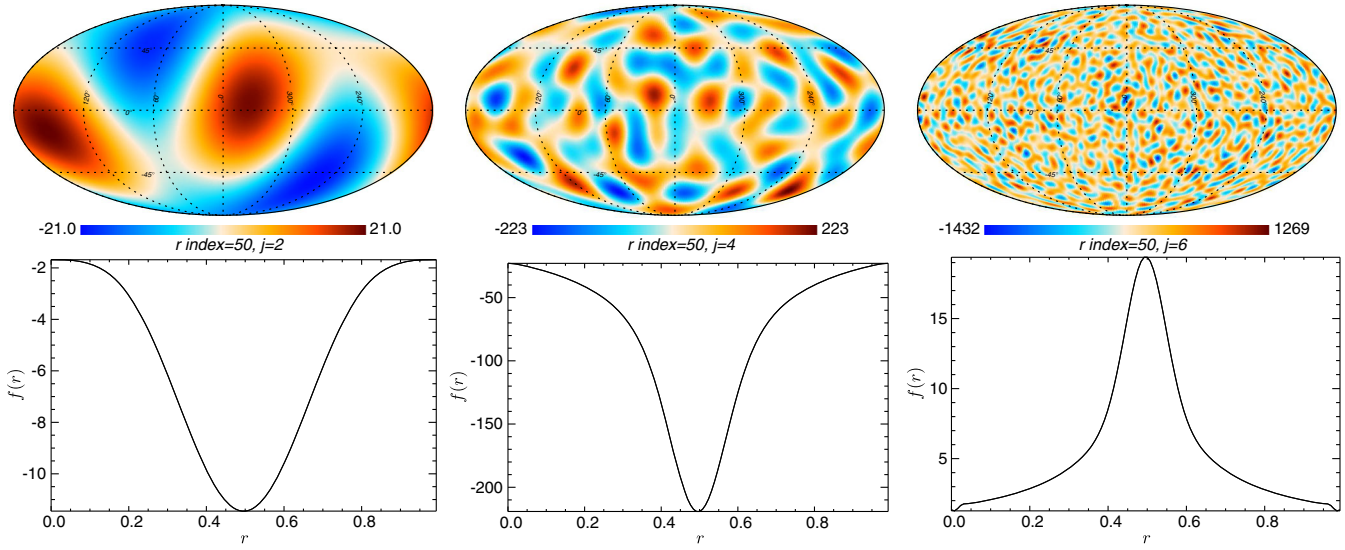

FIG. 4 (color online). 3D-needlet component maps: the upper panel shows the angular part of the corresponding needlet component map at the 51st shell, while the lower panel is for the radial part at the 201 HEALpix pixel. The jth component has a compact support of multipoles $B^{j-1} < \sqrt{\ell(\ell+1)+n^2} < B^{j+1}$.

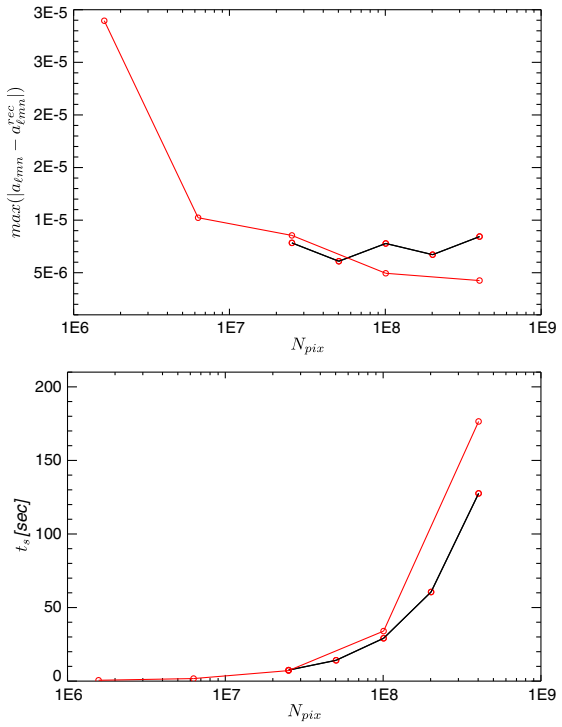

FIG. 5 (color online). Time and accuracy scaling of almn2ball and ball2almn transformations as a function of the total number of ball pixels. The upper panel shows the maximal difference between input and reconstructed $a_{\ell mn}$ coefficients, while the lower panel shows the average time it takes to do synthesis followed by analysis. The black curves correspond to a fixed number of angular pixels, set by HEALpix $N_{\rm side} = 256$, and an increasing number of radial pixels $N_r = 64, 128, 256, 512, 1024$; the red curves correspond to a fixed $N_r = 64$ and $N_{\rm side} = 64, 128, 256, 512, 1024$. We used $\ell_{\rm max} = 2 * N_{\rm side}$ and $n_{\rm max} = N_r/2$.

multipoles used are set to be $\ell_{\rm max} = 2 * N_{\rm side}$ and $n_{\rm max} = N_r/2$. Our reconstruction errors, which are $\sim 10^{-5}$, are mainly determined by the level of accuracy that can be achieved in the HEALpix map2alm_iterative routine. This can be greatly improved by increasing the iteration number.

ACKNOWLEDGMENTS

C. D., Y. F. and D. M. are supported by European Research Council Grant No. Pascal 277742. We thank the two referees for their constructive and useful suggestions and comments.

APPENDIX: SOME TECHNICAL DETAILS

In this Appendix, we discuss the tight frame property that characterizes this construction. Indeed, let $F \in L^2(M, d\mu)$; the corresponding 3D-needlet coefficients are given by (3.4). For all $1 \le q \le Q_j$, $1 \le k \le K_j$, we have

$$|\beta_{j,q,k}|^2 = \lambda_{j,q,k} \left| \sum_{[\ell,n]_j} \sum_{|m|\le \ell} b\left(\frac{\sqrt{e_{\ell,n}}}{B^j}\right) a_{\ell,m,n} u_{\ell,m,n}(\xi_{j,q,k}) \right|^2.$$

From the spectral theorem (see, for instance, Ref. [63], cf. also Ref. [45]), we have also, for $F \in L^2(M, d\mu)$,

$$\sum_{j\in\mathbb{Z}} \|b(B^{-j}\sqrt{\Delta_M})F\|^2_{L^2(M,d\mu)} = \|F\|^2_{L^2(M,d\mu)},$$

where $\|.\|^2_{L^2(M)}$ denotes as usual the L^2 norm of the function that we recalled in (3.3). Let us introduce also the kernel

$$\mathcal{K}_j(x,x') := \sum_{[l,n]_j}\sum_{|m=-l}^{l} b\left(\frac{\sqrt{e_{n,l}}}{B^j}\right)\bar{u}_{\ell,m,n}(x')u_{\ell,m,n}(x),$$

$x, x' \in M$, from which we obtain the projections

$$F_j(x) := b(B^{-j}\sqrt{\Delta_M})F = \langle \mathcal{K}_j(.,x), F(\cdot)\rangle_{L^2(M,d\mu)} = \sum_{[\ell,n]_j}\sum_{|m=-\ell}^{\ell} b\left(\frac{\sqrt{e_{\ell,n}}}{B^j}\right)a_{\ell,m,n}u_{\ell,m,n}(x).$$

Next,

$$\|F_j(x)\|^2_{L^2(M,d\mu)} = \int_M \left|\sum_{[\ell,n]_j}\sum_{|m=-\ell}^{\ell} b\left(\frac{\sqrt{e_{\ell,n}}}{B^j}\right)a_{\ell,m,n}u_{\ell,m,n}(x)\right|^2 d\mu(x).$$

The integrand function clearly belongs to $\Pi_{B^{2(j+1)}}$, i.e., the space of functions that can be expressed as linear combinations of basis elements corresponding to eigenvalues smaller than $B^{2(j+1)}$. For these functions, an exact cubature formula holds, and we get

$$\|F_j(x)\|^2_{L^2(M,d\mu)} = \sum_{q=1}^{Q_j}\sum_{k=1}^{K_j}\lambda_{j,q,k}|F_j(\xi_{j,q,k})|^2.$$

Therefore, we have that

$$\|F\|^2_{L_2(M,d\mu)} = \sum_{j\geq 0}\|b(B^{-j}\sqrt{\Delta_M})F\|^2_{L^2(M,d\mu)} = \sum_{j\geq 0}\|F_j(x)\|^2_{L^2(M,d\mu)} = \sum_{j\geq 0}\sum_{q=1}^{Q_j}\sum_{k=1}^{K_j}|\beta_{j,q,k}|^2,$$

with unitary tightness constant, as claimed.

[1] J. Bobin, F. Sureau, P. Paykari, A. Rassat, S. Basak, and J.-L. Starck, Astron. Astrophys. **553**, 10 (2013).
[2] S. Das *et al.*, Phys. Rev. Lett. **107**, 021301 (2011).
[3] D. Hanson *et al.* (SPTpol Collaboration), Phys. Rev. Lett. **111**, 141301 (2013).
[4] Planck Collaboration, [Astron. Astrophys. (to be published)].
[5] Pierre Auger Collaboration, J. Cosmol. Astropart. Phys. 05 (2013) 009.
[6] ARGO-YBJ Collaboration, Astrophys. J. **779**, 27 (2013).
[7] Fermi-LAT Collaboration and Fermi-GBM Collaboration, Science **343**, 42 (2013).
[8] A. Giuiana *et al.*, Astron. Astrophys. **516**, L11 (2010).
[9] J. A. Aguilar (IceCube Collaboration), Nucl. Phys. B Proc. Suppl. **237**, 250 (2013).
[10] K. M. Gorski, E. Hivon, A. J. Banday, B. D. Wandelt, F. K. Hansen, M. Reinecke, and M. Bartelman, Astrophys. J. **622**, 759 (2005).
[11] J.-P. Antoine, L. Demanet, L. Jacques, and P. Vandergheynst, Appl. Comput. Harmon. Anal. **13**, 177 (2002).
[12] B. Casaponsa, R. B. Barreiro, A. Curto, E. Martínez-Gonzalez, and P. Vielva, Mon. Not. R. Astron. Soc. **411**, 2019C (2011).
[13] S. Donzelli, F. K. Hansen, M. Ligouri, D. Marinucci, and S. Matarreses, Astrphys. J. **755**, 19 (2012).
[14] G. Faÿ, J. Delabrouille, G. Kerkyacharian, and D. Picard, Ann. Appl. Stat. **7**, 1040 (2013).
[15] F. Guilloux, G. Faÿ, and J. F. Cardoso, Appl. Comput. Harmon. Anal. **26**, 143 (2009).
[16] B. Leistedt, J. D. McEwen, P. Vandergheynst, and Y. Wiaux, Astron. Astrophys. **558**, A128 (2013).
[17] J. D. McEwen, P. Vielva, Y. Wiaux, R. B. Barreiro, I. Cayón, M. P. Hobson, A. N. Lasenby, E. Martínez-González, and J. L. Sanz, J. Fourier Anal. Appl. **13**, 495 (2007).
[18] D. Marinucci, D. Pietrobon, A. Balbi, P. Baldi, P. Cabella, G. Kerkyacharian, P. Natoli, D. Picard, and N. Vittorio, Mon. Not. R. Astron. Soc. **383**, 539 (2008).
[19] D. Pietrobon, A. Balbi, and D. Marinucci, Phys. Rev. D **74**, 043524 (2006).
[20] D. Pietrobon, A. Amblard, A. Balbi, P. Cabella, A. Cooray, and D. Marinucci, Phys. Rev. D **78**, 103504 (2008).
[21] O. Rudjord, F. K. Hansen, X. Lan, M. Ligouri, D. Marinucci, and S. Materrese, Astrophys. J. **701**, 369 (2009).
[22] J.-L. Starck, Y. Moudden, P. Abrial, and M. Nguyen, Astron. Astrophys. **446**, 1191 (2006).
[23] J.-L. Starck, Y. Moudden, and J. Bobin, Astron. Astrophys. **497**, 931 (2009).
[24] Y. Wiauz, J. D. McEwen, P. Vandergheynst, and O. Blanc, Mon. Not. R. Astron. Soc. **388**, 770 (2008).
[25] J.-L. Starck, F. Murtagh, and J. Fadili, *Sparse Image and Signal Processing: Wavelets, Curvelets, Morphological Diversity* (Cambridge University Press, Cambridge, England, 2009).
[26] R. Iuppa, G. Di Sciascio, F. K. Hansen, D. Marinucci, and R. Santonico, Nucl. Instrum. Methods Phys. Res. A **692**, 170 (2011).
[27] J. Schmitt, J. L. Starck, J. M. Casandjian, J. Fadili, and I. Grenier, Astron. Astrophys. **546**, A114 (2012).
[28] X. Lan and D. Marinucci, Electron. J. Statist. **2**, 332 (2008).
[29] D. Regan, P. Mukherjee, and D. Seery, Phys. Rev. D **88**, 043512 (2013).

[30] M. Cruz, E. Martínez-Gonzalez, P. Vielva, and L. Cayon, Mon. Not. R. Astron. Soc. **356**, 29 (2005).
[31] P. Vielva and J. L. Sanz, Mon. Not. R. Astron. Soc. **404**, 895 (2010).
[32] S. Scodeller, F. K. Hansen, and D. Marinucci, Astrophys. J. **753**, 27 (2012).
[33] J. Bobin, J.-L. Starck, J.-L. Sureau, and S. Basak, Astron. Astrophys. **550**, A73 (2012).
[34] J. Delabrouille, J.-F. Cardoso, M. Le Jeune, M. Betoule, G. Faÿ, and F. Guilloux, Astron. Astrophys. **493**, 835 (2009).
[35] H. I. Modest, C. Räth, A. J. Banday, G. Rossmanith, R. Sütterlin, S. Basak, J. Delabrouille, K. M. Górski, and G. E. Morfill, Mon. Not. R. Astron. Soc. **428**, 551 (2012).
[36] M. Remazeilles, J. Delabrouille, and J. F. Cardoso, Mon. Not. R. Astron. Soc. **418**, 467 (2011).
[37] R. Laureijs, L. Duvet, I. Escudero Sanz, P. Gondoin, D. H. Lumb, T. Oosterbroek, and G. Saavedra Criado, in *The Euclid Mission, SPIE Proceedings* Vol. 7731 (SPIE-International Society for Optical Engineering, Bellingham, WA, 2010).
[38] V. Springel *et al.*, Nature (London) **435**, 629 (2005).
[39] M. Fengler, D. Michel, and V. Michel, Z. Angew. Math. Mech. **86**, 856 (2006).
[40] V. Michel, PAMM **5**, 775 (2005).
[41] P. Petrushev and Y. Xu, Constr. Approx. **27**, 121 (2008).
[42] F. Lanusse, A. Rassat, and J. L. Starck, Astron. Astrophys. **540**, A9 (2012).
[43] B. Leistedt and J. D. McEwen, IEEE Trans. Signal Process. **60**, 6257 (2012).
[44] D. Geller and A. Mayeli, Math. Z. **263**, 235 (2009).
[45] I. Z. Pesenson, arXiv:1208.5165.
[46] P. Baldi, G. Kerkyacharian, D. Marinucci, and D. Picard, Ann. Stat. **37**, 3362 (2009).
[47] D. Geller and D. Marinucci, J. Fourier Anal. Appl. **16**, 840 (2010).
[48] D. Geller, F. K. Hansen, D. Marinucci, G. Kerkyacharian, and D. Picard, Phys. Rev. D **78**, 123533 (2008).
[49] X. Khalid, R. A. Kennedy, and J. D. McEwen, arXiv: 1403.5553.
[50] F. J. Narcowich, P. Petrushev, and J. D. Ward, J. Funct. Anal. **238**, 530 (2006).
[51] F. J. Narcowich, P. Petrushev, and J. D. Ward, SIAM J. Math. Anal. **38**, 574 (2006).
[52] I. Z. Pesenson, Trans. Am. Math. Soc., **352**, 4257 (2000).
[53] I. Z. Pesenson, J. Geomet. Anal. **14**, 101 (2004).
[54] I. Z. Pesenson and D. Geller, Dev. Math. **28**, 431 (2013).
[55] D. Marinucci and G. Peccati, *Random Fields on the Sphere. Representation, Limit Theorem and Cosmological Applications* (Cambridge University Press, Cambridge, England, 2008).
[56] E. Hernandez and G. Weiss, *A First Course on Wavelets* (CRC Press, Boca Raton, FL, 1996).
[57] I. Z. Pesenson, *Handbook of Geomathematics* (Springer, New York, 2013).
[58] D. Donoho, I. Johnstone, G. Kerkyacharian, and D. Picard, Ann. Stat. **24**, 508 (1996).
[59] W. Hardle, G. Kerkyacharian, D. Picard, and A. Tsybakov, *Wavelets, Approximations and Statistical Application* (Springer, Berlin, 2011).
[60] P. Baldi, G. Kerkyacharian, D. Marinucci, and D. Picard, Ann. Stat. **37**, 1150 (2009).
[61] D. Geller and A. Mayeli, Math. Z. **262**, 895 (2009).
[62] A. Lewis, A. Challinor, and A. Lasenby, Astrophys. J. **538**, 473 (2000).
[63] E. B. Davies, *Spectral Theory and Differential Operators* (Cambridge University Press, Cambridge, England, 1996).